Neutrino decoupling is altered by flavor conversion

Shashank Shalgar and Irene Tamborra
Niels Bohr International Academy and DARK, Niels Bohr Institute,
University of Copenhagen, Blegdamsvej 17, 2100 Copenhagen, Denmark

The large neutrino density in the deep interior of core-collapse supernovae and compact binary merger remnants makes neutrino flavor evolution nonlinear because of the coherent forward scattering of neutrinos among themselves. Under the assumption of spherical symmetry, we model neutrino decoupling from matter in an idealized setup and present the first nonlinear simulation of flavor evolution in the presence of charged current and neutral current collisions, as well as neutrino advection. Within our framework, we find that flavor transformation occurs before neutrinos fully decouple from matter, dynamically affecting the flavor distributions of all neutrino species and shifting the location of the neutrino decoupling surfaces. Our results call for further work as they may have implications on the explosion mechanism of supernovae, the nucleosynthesis of the heavy elements, as well as the observable neutrino signal, all of which is yet to be assessed.

I. INTRODUCTION

Neutrinos are fundamental particles in the physics of core-collapse supernovae [1,2]. Neutrinos are copiously emitted as matter accretes onto the protoneutron star and transport energy and lepton number. According to the delayed neutrino-driven mechanism [3–5], neutrinos are essential to revive the stalled shock wave, powering the explosion. Similarly, in neutrino-cooled disks stemming from the merger of two neutron stars or the collapse of rotating massive stars, neutrinos radiate most of the heat stemming from the turbulent flow, the neutrino pair-annihilation rate may contribute to power the jet of short gamma-ray bursts, and the neutrino-driven outflow launched from the disk contributes, at least partially, to the synthesis of the heavy elements [6–11].

Despite swift progress occurring in the last decade, neutrinos are treated as radiation in hydrodynamic simulations of core-collapse supernovae and compact binary merger remnants [12–16]. However, they should be modeled through a quantum kinetic approach describing the evolution of the distributions of all six neutrino species (three neutrino flavors and their antiparticles), including flavor mixing [17–21]. This approximation is adopted because solving the full quantum kinetic transport of neutrinos is a formidable task, entailing the solution of a seven-dimensional nonlinear problem (involving time, three spatial coordinates, energy, and two angular degrees of freedom), whose characteristic quantities rapidly vary by many orders of magnitude [22–24]. To date, this problem is not solvable with available computational resources.

Flavor evolution depends on the neutrino mixing parameters, as well as on the coherent forward scattering of neutrinos onto each other and on matter [17,25–30]. Neutrino-neutrino interaction makes the equations of motion nonlinear and correlates the flavor evolution of neutrinos of different momenta. A full solution of the quantum neutrino transport problem does not exist yet.

The omission of neutrino conversion in hydrodynamical simulations was not deemed worrisome in supernovae as it was expected to occur beyond the shock radius, and thus, not having an impact on the shock revival [31]. However, this picture has been shaken by recent developments [32–36], hinting that neutrino conversion could already develop in the proximity of the neutrino decoupling region [37–47], with a characteristic timescale that is proportional to the number density of neutrinos and antineutrinos (hence dubbed "fast" to distinguish it from the "slower" conversion driven by the vacuum frequency). The impact of flavor conversion on the supernova physics remains to be understood. Additionally, in compact binary mergers, flavor conversion could affect the disk cooling rate as well as the neutron-to-proton ratio [48–52].

In the context of fast flavor conversion, an important role is played by the angular distributions of (anti)neutrinos: a crossing between the angular distributions of ν_e and $\bar{\nu}_e$, or a change of sign in the electron neutrino lepton number (ELN) within a certain angular range, constitutes a necessary

condition to trigger a flavor instability [36,53,54], in the limit of vanishing mass-squared difference [24,32,34,36,38,55–60]. The amount of induced flavor conversion is, however, unknown [61]. In the light of these developments, it becomes of paramount importance to ascertain whether the presence of ELN crossings is modified by flavor conversion and vice versa.

In the supernova core, for example, neutrinos are trapped with a mean-free path of $\mathcal{O}(10)$ m at typical baryon densities of $\mathcal{O}(10^{14})$ g/cm^3 [62]. As the distance from the supernova increases and the baryon density decreases, neutrinos start decoupling from matter. However, not all flavors of neutrinos decouple simultaneously due to the flavor dependent cross section of neutrinos. Their angular distributions are initially almost isotropic and, as the density decreases, become forward peaked and ELN crossings can form, also because of collisions and advection [46,63]. Recent work shows that, if flavor conversion should occur in the decoupling region, a nontrivial feedback between neutrino flavor transformations and collisions could take place [63–70]. Similarly, neutrino advection and the spatial dimensionality of the problem could also dynamically modify the conditions for flavor conversion [56,71].

In this paper, we present the first investigation of flavor conversion as the angular distributions of neutrinos evolve in the collisional regime within an idealized toy-model shell and in the presence of neutrino advection. Our work is organized as follows. We introduce the mean field equations of motion in Sec. II, together with the modeling of the collision term. The decoupling of neutrinos in the absence and then in the presence of flavor conversion is discussed in Secs. III and IV, respectively. Section V focuses on the interplay between slow and fast conversion. The characteristic timescales of the problem are instead discussed in Sec. VI. Finally, our findings are summarized in Sec. VII. The Appendix provides additional material comparing simulations with our standard resolution with others obtained with a smaller number of bins in radius.

II. MEAN FIELD EQUATIONS OF NEUTRINOS

In this section, we introduce the kinetic equations of neutrinos. We also outline our modeling of the collision term, which mimics the hierarchy of decoupling of the different neutrino flavors, despite being heuristic.

A. Kinetic equations

For the sake of simplicity, we work in the two-flavor approximation, i.e. in the (ν_e, ν_x) basis [57,59,72,73]. The [anti]neutrino field is described through a 2×2 density matrix, $\rho(\vec{r}, \vec{p}, t)$ $[\bar{\rho}(\vec{r}, \vec{p}, t)]$. The diagonal elements of the density matrix (ρ_{ii}, with $i = e, x$) represent the occupation numbers of neutrinos of different species, while the off-diagonal terms (ρ_{ij}) encode flavor coherence. The

evolution of the neutrino field at time t, location $\vec{r}$ and momentum $\vec{p}$ is governed by the following equation [74]:

$$\left(\frac{\partial}{\partial t} + \vec{v} \cdot \vec{\nabla} \right) \rho(\vec{r}, \vec{p}, t) = \mathcal{C} - i[H(\vec{r}, \vec{p}, t), \rho(\vec{r}, \vec{p}, t)]. \quad (1)$$

We work in spherical symmetry and assume only one energy mode E; hence, $\rho(\vec{r}, \vec{p}, t) = \rho(r, E, \theta, t)$, with θ being the local polar angle defined with respect to the radial direction and at a given r. On the left-hand side of Eq. (1), the advective term is

$$\vec{v} \cdot \vec{\nabla} = \cos\theta \frac{\partial}{\partial r} + \left(\frac{\sin^2\theta}{r} \right) \frac{\partial}{\partial \cos\theta}, \quad (2)$$

in agreement with e.g., Refs. [75,76].

The commutator on the right-hand side of Eq. (1) encodes the flavor evolution of neutrinos. The Hamiltonian, $H = H_{\text{vac}} + H_{\text{matt}} + H_{\nu\nu}$, governs the coherent evolution of neutrinos and is composed of the vacuum and neutrino self-interaction term,

$$H_{\text{vac}} = \frac{\omega}{2} \begin{pmatrix} -\cos 2\vartheta_{\text{V}} & \sin 2\vartheta_{\text{V}} \\ \sin 2\vartheta_{\text{V}} & \cos 2\vartheta_{\text{V}} \end{pmatrix}, \quad (3)$$

$$H_{\nu\nu} = \mu_0 \int [\rho(\cos\theta') - \bar{\rho}(\cos\theta')]$$
$$\times (1 - \cos\theta\cos\theta') d\cos\theta', \quad (4)$$

where we have absorbed the constant factor coming from the integration over the azimuthal angle in μ_0 and suppressed the dependence on r and t for the sake of brevity. The term, H_{matt}, linked to matter effects should also appear in H. However, the effect of the matter potential is to suppress the vacuum mixing angle ϑ_V [77], hence we set $H_{\text{matt}} = 0$ and use $\vartheta_V = 10^{-3}$ instead.[1] The vacuum frequency is $\omega = \Delta m^2/2E$, with Δm^2 being the squared mass difference. For antineutrinos, $\omega \to -\omega$ in H_{vac}, while all other terms of H remain unchanged.

B. The collision term

The collision term in Eq. (1), $\mathcal{C} \equiv \mathcal{C}(\vec{r}, E, t) = \mathcal{C}_{\text{emission}} + \mathcal{C}_{\text{absorb}} + \mathcal{C}_{\text{dir-ch}}$, includes emission, absorption, and direction-changing collisions, respectively [78]. It encapsulates all the reactions of neutrinos with the matter background [13,63,79,80]. We assume that the collision term only affects the diagonal components of

TABLE I. Inverse length-scales associated with emission, absorption and direction-changing scattering for all the flavors (see Eqs. (5)–(7). The function $\xi(r) = \exp(-(r-15)/\text{km})$ ensures that the collision term vanishes at large distances.

	ν_e	$\bar{\nu}_e$	$\nu_x, \bar{\nu}_x$
$\lambda^{\nu_i}_{\text{emission}}$ (km)	$1/[50\xi(r)]$	$1/[50\xi(r)]$	$1/[10\xi(r)]$
$\lambda^{\nu_i}_{\text{absorb}}$ (km)	$1/[50\xi(r)]$	$1/[50\xi(r)]$	$1/[10\xi(r)]$
$\lambda^{\nu_i}_{\text{dir-ch}}$ (km)	$1/[50\xi(r)]$	$1/[25\xi(r)]$	$1/[12.5\xi(r)]$

the density matrices,[2] as the timescales associated with flavor evolution are shorter than the collision ones [24].

For the sake of simplicity, given that we intend to explore the interplay between the neutrino decoupling and the flavor conversion for the very first time, we rely on a heuristic collision term, that allows for neutrinos to transition from the trapping regime to free streaming within a small spatial range (i.e., [15, 30] km in our simulations, while providing decoupling regions and decoupling hierarchy among the different flavors inspired by Ref. [37]), since we are limited by the size of our simulation shell due to technical complications induced by the treatment of flavor conversion. For simplicity, we retain the dependence of $\mathcal{C}$ on r and neglect its angular dependence because it is dominated by the interaction of neutrinos with nucleons that are heavier than the neutrino average energies:

$$\mathcal{C}^{\nu_e, \bar{\nu}_e, \nu_x, \bar{\nu}_x}_{\text{emission}} = \frac{1}{\lambda^{\nu_e, \bar{\nu}_e, \nu_x, \bar{\nu}_x}_{\text{emission}}(r)}, \tag{5}$$

$$\mathcal{C}^{\nu_e, \bar{\nu}_e, \nu_x, \bar{\nu}_x}_{\text{absorb}} = -\frac{1}{\lambda^{\nu_e, \bar{\nu}_e, \nu_x, \bar{\nu}_x}_{\text{absorb}}(r)} \rho_{ii}(\cos\theta), \tag{6}$$

$$\mathcal{C}^{\nu_e, \bar{\nu}_e, \nu_x, \bar{\nu}_x}_{\text{dir-ch}} = -\frac{2}{\lambda^{\nu_e, \bar{\nu}_e, \nu_x, \bar{\nu}_x}_{\text{dir-ch}}(r)} \rho_{ii}(\cos\theta)$$
$$+ \int_{-1}^{1} \frac{1}{\lambda^{\nu_e, \bar{\nu}_e, \nu_x, \bar{\nu}_x}_{\text{dir-ch}}(r)} \rho_{ii}(\cos\theta') d\cos\theta'. \tag{7}$$

Each of the above equations refers to all flavors as denoted by the superscripts, and the flavor-dependent length scales, λ^{ν_i}, are tabulated in Table I and shown in Fig. 1. Equations (5) and (6) determine the rate at which neutrinos traveling in the direction θ are created and absorbed, respectively. Equation (7) represents the probability that a neutrino traveling along θ' will change to the θ direction. While Eqs. (5) and (6) do not conserve the number of neutrinos, Eq. (7) preserves the number of neutrinos.

---

[2]We have tested that the inclusion of the off-diagonal components of the collision terms following the method adopted in Ref. [76] results in a negligible error on the final flavor configuration (the relative error averaged over the radius is 2.2%).
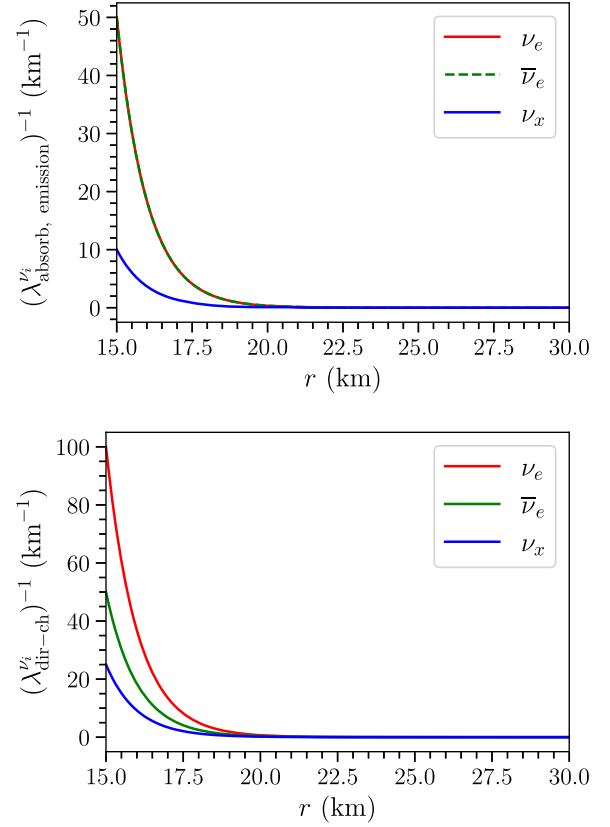

FIG. 1. Inverse length scales associated with emission, absorption, and direction-changing scattering for ν_e (in red), $\bar{\nu}_e$ (in green), and ν_x (in blue) as functions of radius. The functional forms of these terms are reported in Table I, see also Eqs. (5)–(7).

In our simulations, neutrinos of all flavors are generated through collisions. The ratio between $\mathcal{C}_{\text{emission}}$ and $\mathcal{C}_{\text{absorb}}$ determines ρ_{ii} for all flavors at $r_{\min} = 15$ km. Since only $\mathcal{C}_{\text{emission}}$ and $\mathcal{C}_{\text{absorb}}$ play a role in the trapping regime, the number density at $r_{\min}$ can be determined analytically in the steady-state configuration. At larger r, $\mathcal{C}_{\text{dir-ch}}$ also comes into play in shaping the angular distributions and no analytical solution exists. In addition, in our simplified setup, we neglect Pauli blocking [81,82] and assume that the neutrino chemical potentials are negligible.

To investigate the decoupling of neutrinos, we focus on the simulation shell from 15 km to 30 km. We use 7500×150 bins in r and $\cos\theta$, respectively. Additional technical details on the numerical implementation and convergence are provided in Secs. III and VI, as well as the Appendix and Ref. [83].

The radial profiles for the heuristic collision terms are shown in Fig. 1 (see also Table I). We can see that $\lambda^{-1}_{\text{dir-ch}}$ is the largest contribution for all flavors at small radii. The direction changing scattering is dominated by neutral current interactions with nucleons. Because of our single energy approximation, we adopt an heuristic approach to model the collision term such that ν_e's have the smallest mean-free path, while nonelectron type neutrinos have the
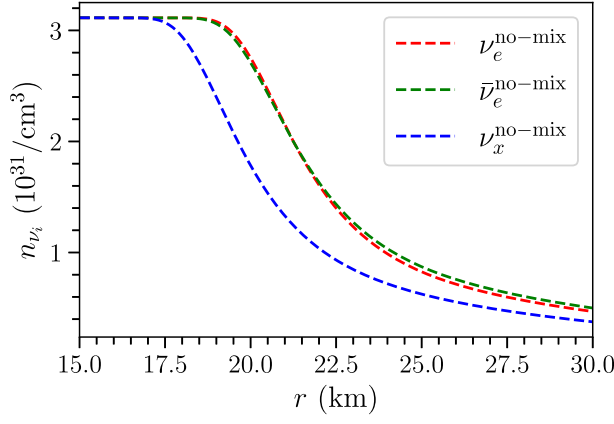
FIG. 2. Neutrino number densities of ν_e (in red), $\bar{\nu}_e$ (in green), and ν_x (in blue) as functions of radius in the steady-state configuration in the absence of neutrino mixing. The number density has no radial dependence in the trapping regime ($r \lesssim 18$ km), while it falls of like $1/r^2$ at larger radii ($r \gtrsim 25$ km), as expected because the absorption and emission terms are very small.

longest mean-free path, as expected [13,79,80]. Moreover, the fact that the $\bar{\nu}_e$ mean-free path is larger than the ν_e one ensures that the $\bar{\nu}_e$'s decouple at a smaller radius than ν_e's [84,85]. As the radius increases, all inverse length scales decrease, until they are negligible for $r \gtrsim 25$ km, when neutrinos decouple from matter as shown in the top panel of Fig. 3.

As neutrinos start to decouple from matter, the angular distribution for each neutrino flavor becomes forward peaked and the number density which is proportional to the diagonal components of the density matrix falls off. This is clearly visible from the radial profile of the number density for each flavor [which corresponds to $n_{\nu_i}(r) = \mu_0 \int_{-1}^{1} \rho_{ii}(r, \cos\theta) d\cos\theta / (\sqrt{2}G_F)$ in physical units] shown in Fig. 2, in the steady-state configuration and in the absence of neutrino mixing. At radii larger than ~ 25 km, the emission and absorbtion terms are almost zero. In this limit we find that the neutrino number density falls off like $1/r^2$ as expected due to conservation of neutrino number for each flavor. Also, since there is almost no absorption or emission of neutrinos in the region of $r \gtrsim 25$ km, the angular distributions become forward peaked as the only neutrinos that are present at these radii are the ones which have escaped the core and travel along directions that are close to the radial one.

III. NEUTRINO DECOUPLING IN THE ABSENCE OF FLAVOR CONVERSION

For all the simulations presented in this paper, we use the central difference method for spatial derivatives, while an adaptive multistep Adams-Bashforth-Moulton method is adopted for the temporal evolution with absolute and relative tolerances of 10^{-12}. The central difference method
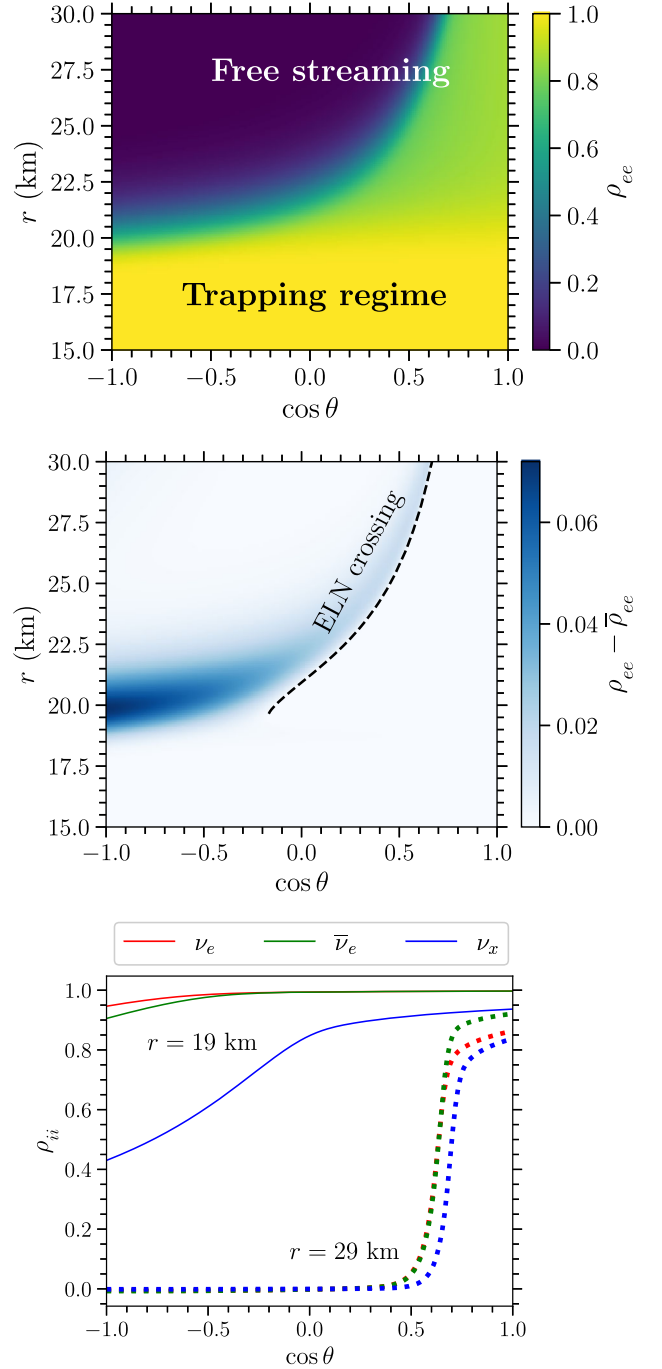

FIG. 3. Steady-state neutrino-flavor configuration in the absence of flavor mixing. These distributions [generated by imposing $H = 0$ in Eq. (1) and extracted at $t = 10^{-4}$ s] are the ones adopted as input to investigate the effects of flavor conversion. Top panel: Contour plot of ρ_{ee} (proportional to the ν_e number density) in the plane spanned by $\cos\theta$ and r. Middle panel: Same as in the top panel but for $\rho_{ee} - \bar{\rho}_{ee}$ (proportional to the ELN density). The dashed line marks the region where ELN crossings develop. Bottom panel: Angular distributions of ν_e, $\bar{\nu}_e$, and ν_x at $r = 19$ km (solid) and 29 km (dotted). As r increases, the angular distributions become prominently forward peaked in a flavor-dependent fashion and ELN crossings develop.

adopted to calculate the spatial derivative and the derivatives with respect to $\cos \theta$ cannot be applied to the edges of the simulation shell and hence to the related derivatives. As for the derivative with respect to $\cos \theta$, we use the forward and backward difference method at $\cos \theta = -1$ and $\cos \theta = 1$, respectively. For $r = r_{min}$, the boundary condition is set by requiring a classical steady-state solution. For $r = r_{max}$, there are two distinct domains that need to be considered independently. For $\cos \theta > 0$, neutrinos travel outwards and, therefore, the boundary condition does not need to be specified. For $\cos \theta < 0$, the neutrino flux for all flavors is set to zero.

The kind of ELN crossing could affect the development of flavor-conversion physics [24,42]. We choose a representative case in this work. However, we investigate the flavor-conversion physics for a set of different ELN crossings (i.e., different collision terms) in Ref. [83] and show that our main conclusions are not qualitatively affected.

The flavor configuration displayed in Fig. 3 represents the classical steady-state configuration obtained in the absence of neutrino flavor transformation. Within our setup, the neutrino angular distributions are populated through collisions and advection across the simulation shell. While we rely on heuristic collision terms and focus on an idealized simulation shell, the decoupling regions and the hierarchy among the different flavors qualitatively reproduce the ones obtained from hydrodynamical simulations, e.g., Ref. [37], while also developing ELN crossings.

The decoupling of neutrinos from matter is driven by the flavor-dependent collision term along with neutrino advection [63,86]. Solving Eq. (1) for $H = 0$ (i.e. in the absence of flavor conversion) and no neutrinos in the simulation shell at $t = 0$, the collision terms in Eqs. (5)–(7) lead to a steady-state configuration for each neutrino species after a sufficiently large time interval ($t \gtrsim 10^{-4}$ s). The top panel of Fig. 3 shows a contour plot of ρ_{ee} in the plane spanned by $\cos \theta$ and r. At small radii, the angular distribution (15 km $\lesssim r \lesssim$ 18 km) is uniform in $\cos \theta$; as r increases, the angular distribution becomes gradually forward peaked and its backward part ($\cos \theta \lesssim 0$) is progressively emptied as full decoupling is reached. A similar behavior holds for all (anti)neutrino species.

As the presence of ELN crossings is crucial to the development of fast flavor conversion, the middle panel of Fig. 3 displays a contour of $\rho_{ee} - \bar{\rho}_{ee}$ in the plane spanned by $\cos \theta$ and r. ELN crossings are not prominent at small r, but they develop at $r \gtrsim 18$ km and affect different angular regions as r increases. The dark blue band to the left of the dashed line in Fig. 3 is the region with an excess of ν_e over $\bar{\nu}_e$ due to the fact that the $\bar{\nu}_e$ decoupling radius is smaller than the ν_e one. The bottom panel of Fig. 3 displays snapshots of the angular distributions of ν_e, $\bar{\nu}_e$, and $\nu_x = \bar{\nu}_x$ at two representative radii. As $\mathcal{C}$ evolves as a function of r,

the angular distribution of each flavor becomes forward peaked and ELN crossings are visible.

The dashed lines in the top panel of Fig. 4 show the radial evolution of the angle-averaged occupation number for ν_e and ν_x. In order to determine the decoupling surface, we compute the flux factor,

$$\mathcal{F}_{\nu_i} = \frac{\int_{-1}^{1} \rho_{ii}(\cos \theta) \cos \theta \, d\cos \theta}{\int_{-1}^{1} \rho_{ii}(\cos \theta) d\cos \theta}, \qquad (8)$$
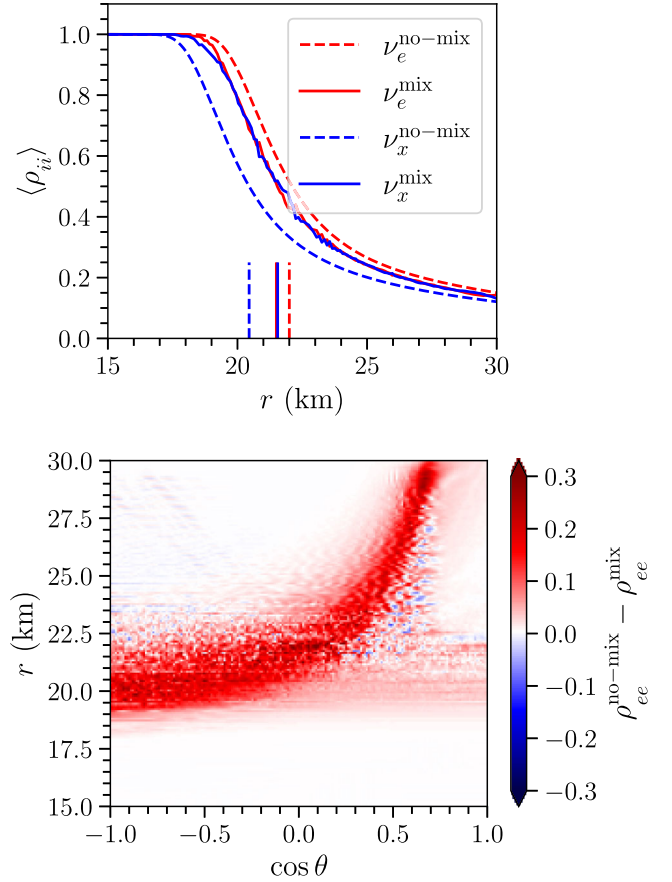

FIG. 4. Steady-state neutrino flavor configuration in the presence of flavor mixing (extracted 5×10^{-5} s after the classical steady-state configuration is reached in our simulation). Top: Angle averaged neutrino occupation numbers of ν_e (in red) and ν_x (in blue) with (solid lines) and without (dashed lines) neutrino mixing as functions of the radius. The vertical lines mark the radii of decoupling (approximately defined as the radius at which $\mathcal{F}_{\nu_i} = 1/3$). A similar trend holds for antineutrinos; however, note that flavor conversion induces a difference between ν_x and $\bar{\nu}_x$. Bottom: Contour plot of the difference between the ν_e occupation number without (when the classical steady-state configuration is achieved) and with neutrino mixing in the plane spanned by $\cos \theta$ and r. Due to the collective nature of the neutrino flavor evolution and flavor lepton number conservation, the corresponding heatmap for antineutrinos looks very similar and is not shown.

and approximately define the radius of decoupling as the radius at which the flux factor is $\mathcal{F}_{\nu_i} = 1/3$ [37,49]. The corresponding decoupling surfaces of ν_e and ν_x are shown in the top panel of Fig. 4.

IV. NEUTRINO DECOUPLING IN THE PRESENCE OF FLAVOR CONVERSION

Switching on flavor mixing in Eq. (1) (i.e., $H \neq 0$), we assume that neutrinos have $\omega = 0.32$ km^{-1}, which corresponds to $E = 20$ MeV for $\Delta m^2 = 2.5 \times 10^{-3}$ eV^2, and $\mu_0 = 10^4$ km^{-1}. We adopt the steady-state flavor configuration in Fig. 3 as the initial state.

Figure 4 shows fascinating insights into the effect of flavor conversion on neutrino decoupling. The solid lines in the top panel of Fig. 4 show the angle averaged occupation numbers of ν_e and ν_x. With respect to the case without flavor conversion (dashed lines in Fig. 4), we see that flavor conversion pushes the distributions of ν_e and ν_x towards each other, sensibly modifying them with respect to the case without flavor conversion. However, we stress that flavor equipartition is not a general outcome, but it is linked to the specific flavor setup adopted in this paper; we have found other flavor configurations that do not lead to flavor equipartition (results not shown here), see also Refs. [83,87]. The impact of neutrino flavor evolution is evident in the shift of the radius at which the angle-averaged ρ_{ee} and ρ_{xx} start falling, with consequences on the decoupling radius.

One of the consequences of neutrino flavor conversion is a shift in the radius of neutrino decoupling. The top panel of Fig. 4 shows the flavor-dependent decoupling surfaces with (solid) and without (dashed) flavor conversion for comparison. It is also important to note that neutrinos start to change their flavor at radii much smaller than their decoupling surfaces; this is in stark contrast with the approximation of flavor-independent neutrino-sphere commonly adopted in the literature [22,23,26–29], under the naive expectation that flavor evolution near the neutrinosphere would not be present due to collisional damping [88–90].

The bottom panel of Fig. 4 represents the difference in the ν_e occupation number in the absence and presence of neutrino mixing. As r increases, a region with a deficit of ν_e forms due to flavor conversion (red band). This physics cannot be captured by any calculation that does not include advection and collision, together with flavor transformation (see Fig. 5 and the animations for comparison).

After obtaining a steady-state configuration for all flavors (see Fig. 4), we switch on flavor conversion and explore its interplay with neutrino advection and collisions. In order to highlight the dynamical effects of neutrino advection and collisions on flavor conversion, we show in Fig. 5 the correspondent flavor outcome obtained by switching off collisions and advection once
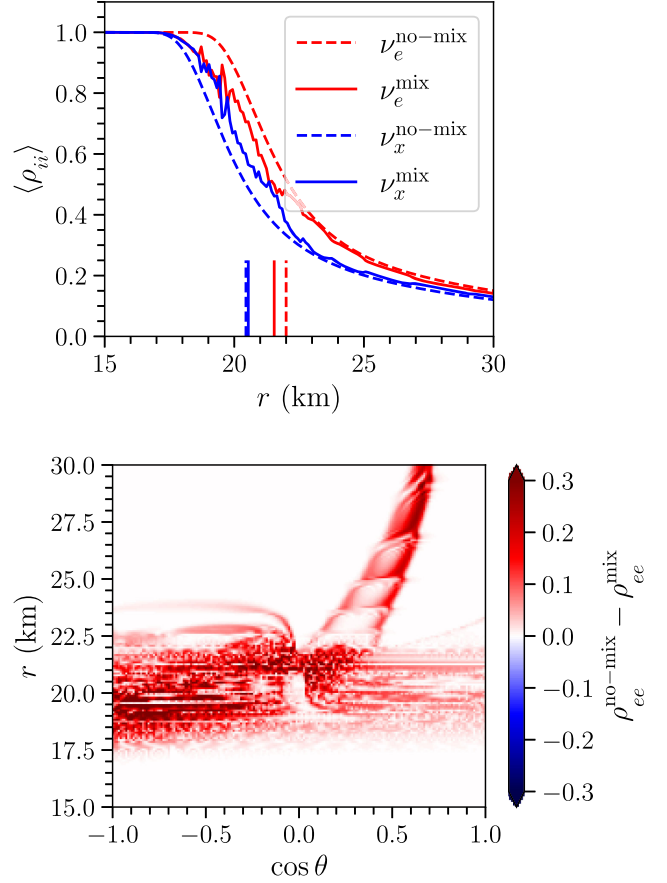

FIG. 5. Final flavor configuration obtained by switching on flavor mixing, after the classical steady state is reached, and switching off collisions and neutrino advection [i.e., $H \neq 0$, $\mathcal{C} = 0$, and $\vec{v} = 0$ in Eq. (1)]. The top and bottom panels are the analogous of the ones in Fig. 2, which instead take into account the dynamical effects on flavor mixing due to collisions and advection [i.e., $H \neq 0$, $\mathcal{C} \neq 0$, and $\vec{v} \neq 0$ in Eq. (1)].

the steady-state flavor configuration is achieved, i.e., by letting flavor transformation operate in the absence of collisions and advection.

From Fig. 5, one can see that collisions and neutrino advection not only affect the final angle-integrated flavor configuration, but also allow to spread the flavor instabilities across angular regions and spatial ranges [56,64,65]. It is also worth noticing that the absence of neutrino advection makes the evolution of neutrino flavor much more oscillatory in nature.

V. INTERPLAY BETWEEN SLOW AND FAST FLAVOR INSTABILITIES

Interestingly, despite the presence of ELN crossings and because of the shape of our ELN angular distributions (see middle panel of Fig. 3) only a small radial range centered on $r \simeq 21$ km is affected by flavor instabilities in the limit of $\omega = 0$ (i.e., when only fast conversion occurs). Because of $\omega \neq 0$ and the system setup, slow collective neutrino

transformations are also triggered at high densities, in contrast to what is commonly assumed in the literature.

In this section, we choose to carry out the linear stability analysis for the homogeneous mode only, as an illustrative example. However, the numerical simulations automatically take into account all modes. Hence, the interplay between slow and fast conversion is accounted for all modes consistently in the numerical simulations. The investigation of the interplay between fast and slow instabilities for nonhomogeneous modes would require the development of a novel analytical framework because of the importance of the scattering terms in our system setup; this task is left to future dedicated work.

The linear stability analysis consists of linearizing the equations of motion and calculating the growth rate of the flavor instability [91]. By setting the collision and the advective terms to zero ($\vec{v} = 0$), expanding Eq. (1) in the off-diagonal component, and ignoring $\mathcal{O}(\rho_{ex}^2)$ and higher-order terms, the solutions are of the form,

$$\rho_{ex}(\cos\theta, t) \sim \exp(-i\Omega t)\rho_{ex}(\cos\theta, 0), \qquad (9)$$

$$\bar{\rho}_{ex}(\cos\theta, t) \sim \exp(-i\Omega t)\bar{\rho}_{ex}(\cos\theta, 0). \qquad (10)$$

The collective nature of flavor evolution ensures that the eigenvalue Ω is the same for neutrinos and antineutrinos and also the same for all values of $\cos\theta$. When a flavor instability is present, Ω has a positive imaginary component, called growth rate and denoted by κ. It should be noted that, although the complex eigenvalues are always present in complex conjugate pairs in the absence of the collision term, this is not the case in the presence of collisions [92], which we do not consider here. However, the presence of a neutrino flavor instability does not necessarily imply significant flavor transformation [93].

Figure 6 shows the growth rate as a function of radius for $\omega = 0$ (fast conversion) and $\omega = 0.32$ km^{-1} adopted in our work. Interestingly, for most of the radial range, the neutrino flavor instability does not exist for $\omega = 0$ for the homogeneous mode because of the shape of our ELN distributions. This implies that initially the neutrino flavor evolution is not driven by ELN crossings, but by the vacuum term for $k = 0$. Fast-flavor instabilities are only present in a small radial range around ~21 km. In addition, once triggered, fast-flavor mixing is further affected by the vacuum frequency [55]. We stress that these findings imply an interplay between fast and slow conversion and do not intend to suggest that the slow modes are dominant for any k. By comparing Fig. 6 with Figs. 4 and 5, we note that although the neutrino flavor instability exists for $r \gtrsim 18$ km, the magnitude of the neutrino-flavor transformation is not directly correlated to κ, in agreement with the findings of Ref. [93] in the context of fast-flavor transformation.
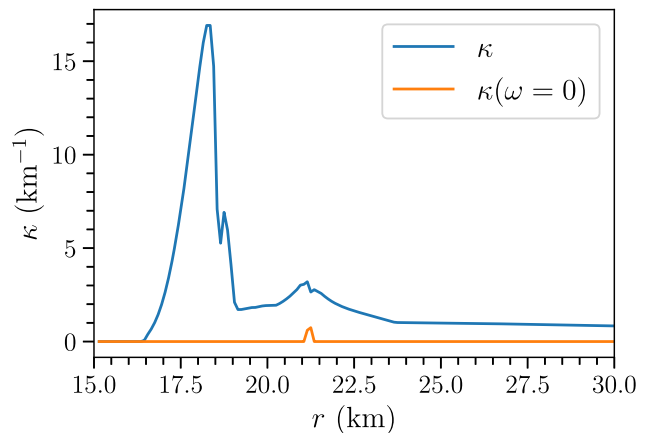

FIG. 6. Growth rate of the flavor instability as a function of radius obtained by adopting the steady-state flavor distributions. The orange line shows the growth rate for $\omega = 0$ (fast conversion), whereas the blue line shows the growth for $\omega = 0.32$ km^{-1} (slow conversion). Contrary to expectations, flavor mixing is induced by slow instabilities; fast-flavor instabilities are only present around ~21 km.

VI. CHARACTERISTIC SCALES OF THE PROBLEM

In the context of fast conversion, the timescale of flavor evolution can be as large as μ^{-1} in special cases (e.g., for $\omega = 0$ and in the absence of collisions and advection). For more realistic cases the timescales are smaller by a few orders of magnitude.

One might naively confuse the timescale with the length scale over which spatial structure is present and in turn assume that this would infer the spatial resolution required to perform a reliable numerical study. However, as demonstrated in Ref. [93], we stress that spatial and temporal scales are not identical when advection is taken into account; it is possible to get reliable results by coarse graining over the small spatial structure, if the latter is at all present, and reproduce the average flavor ratio, see also the Appendix and Ref. [93]. The typical length scale of our problem should not be considered to be $\mathcal{O}(\mu_0^{-1})$, as in e.g., Refs. [71,87,94–96]; these works rely on a different system setup, with structures at length scales of $\mathcal{O}(\mu_0^{-1})$ and periodic boundary conditions that may lead to cascades to smaller length scale with time [97].

In our case, the characteristic length scale of the problem is determined by the flavor-conversion one, as well as the collision and advection scales. If neutrinos were assumed to be emitted by a single surface, as sketched in the left panel of Fig. 7, the typical length scale of the problem would be given by the product of the flavor-conversion timescale and the speed of light (i.e., the advection velocity). This would be the length scale seen in a setup similar to the neutrino-bulb model, where the decoupling region has an infinitesimal extent. However, our decoupling region is much more extended than the oscillation length scale, see right panel of
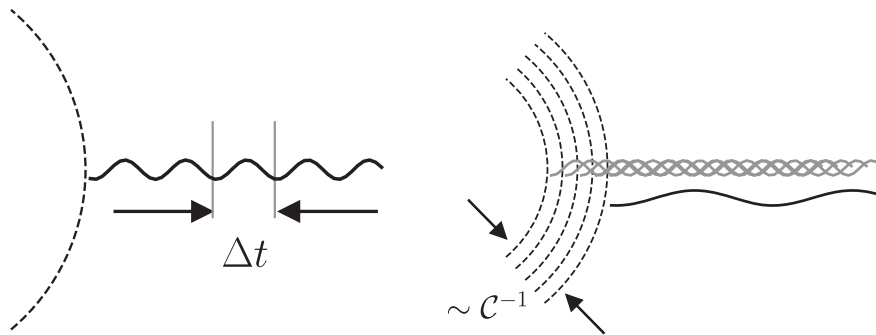
FIG. 7.   Schematic representation of neutrinos being emitted by a decoupling region with infinitesimal extent (left panel) and neutrinos emitted from an extended decoupling region composed of multiple emitting surfaces, each separated from the former and the following one by $\mathcal{O}(\mathcal{C}^{-1})$. For a density profile that is rapidly decreasing, the decoupling region has a width that roughly scales as $\sim\mathcal{C}^{-1}$ (right panel). In the first case, the typical length scale of the neutrino oscillation pattern is given by the product of the flavor conversion timescale Δt and the advection velocity. When an extended decoupling region is considered, the resultant oscillation pattern (black curve) is given by the superposition of multiple oscillation patterns (gray curves), each separated from the other ones by $\mathcal{O}(\mathcal{C}^{-1})$.

Fig. 7. Hence, at a given point, the resultant neutrino field is given by the neutrinos emitted from various locations in the decoupling region (i.e., the small-scale structures that one would see when considering one single emitting surface are smeared as a result of the superposition of oscillating patterns overlapping with each other, as sketched in the right panel of Fig. 7).

For a density profile that is rapidly decreasing, as ours, the extent of the decoupling region is roughly determined by the inverse of the collision term, $\sim\mathcal{C}^{-1}$. Although it is not possible to estimate *a priori* the exact length scale associated with the neutrino field in the presence of flavor transformation, it is clear that the resultant length scale should be between the oscillation and the collision length scales. In summary, μ_0^{-1} constitutes the minimum length scale expected for flavor conversion, the maximum being the collision length scale. As a consequence spatial resolution of $\mathcal{O}(\mu_0^{-1})$ may not be needed for numerical convergence because of the interplay of flavor conversion with collisions and advection.

VII. OUTLOOK

For the first time, we follow the flavor evolution while neutrinos decouple in an idealized shell, in the presence of collisions and advection. We find that neutrino flavor conversion occurs well before all flavors decouple from the matter background and the neutrino decoupling surfaces are affected by flavor transformation.

While dealing with flavor transformation, advection and collisions simultaneously, the collision term adopted in this work relies on heuristic functions that allow us to transition from uniform to forward peaked neutrino distributions within a small spatial region because of the technical challenges induced by the treatment of flavor conversion in the stellar core. A further exacerbation of our findings could be determined by the inclusion of all six flavors, the

energy dependence of the neutrino distributions, and the azimuthal emission angle of neutrinos [55,57,71–73,98]. Additional effects on the decoupling physics may arise from relaxing the assumption of spatial homogeneity [99]. Not only can spatial inhomogeneity lead to additional flavor instabilities, neutrino advection causes dynamical effects which can only manifest in an inhomogeneous system [56].

Despite its caveats and the idealized simulation setup, this work clearly demonstrates that the neutrino decoupling physics is affected by flavor transformation, with possible implications on the neutrino energy deposition in the supernova gain layer and the physics of compact merger remnants that remain to be assessed. The fact that the dynamics of neutrino decoupling changes due to neutrino flavor transformation implies that the neutrino properties at the radius of decoupling may be different from the ones usually computed in hydrodynamic simulations treating neutrinos as radiation. However, a robust assessment of the radiated neutrino spectra in the presence of flavor conversion will have to take into account the hydrodynamic feedback on the thermodynamic properties and a more realistic implementation of the collision term. The occurrence of flavor conversion in the vicinity of the flavor-dependent neutrinospheres puts in perspective the existing literature naively assuming flavor-independent neutrinospheres and a larger radius for the onset of flavor conversion.

APPENDIX: COMPARISON WITH SIMULATIONS WITH SMALLER SPATIAL RESOLUTION

In this appendix we perform a simulation with a smaller number of spatial bins (150) with respect to the one used in the main text. In order to do so, we consider our benchmark system and perform simulations with the self-interaction strength at $r_{\min}$ being $\mu_0 = 10^4$, 10^3, and 10^2 km^{-1} with 150 spatial bins and compare the results with simulations performed with 7500 spatial bins adopted in the main text (i.e., 50 times higher spatial resolution). The choice of a smaller μ_0 allows us to perform numerical simulations with a spatial resolution that is accurate enough to resolve length scales of the order of μ_0^{-1} or smaller.

Figure 8 shows results for $\mu_0 = 10^4$ km^{-1} for our two simulations with 150 and 7500 radial bins (same as the one presented in the main text), with all other simulation inputs unchanged with respect to our benchmark model (including the number of angular bins kept fixed to 150). The top panel shows the difference in the electron neutrino number density, with and without flavor conversion obtained using 150 spatial bins. Despite the appearance of small scale structure due to the coarser graining in radius, the results are same as the ones presented in Fig. 4 within reasonable numerical errors. This is evident from the middle panel of Fig. 8, where we show the comparison between the number densities averaged over angle for the simulations with 150 and 7500 spatial bins. The bottom panel of Fig. 8 displays the relative error between the two simulations. The error averaged over the radial range is 1.1%. This shows that 150 spatial bins are sufficient to capture the main features of the flavor evolution, despite the appearance of small scale structures.

Figure 9 shows a comparison between simulations using smaller values of μ_0 (100 and 1000 km^{-1}, left and right panels, respectively). From the bottom panels, we can see that the average relative error is 1.66% and 1.63% for $\mu_0 = 100$ and 1000 km^{-1}, respectively.

In all cases, the average relative error between the simulations with 150 and 7500 radial bins can reach up to 4–5% in a few radial bins but on average is less than 1–2%. The relative error has been computed by coarse graining the results with 7500 radial bins and averaging over batches of 50 radial bins, to compare the results with the ones from the numerical simulation that used 150 radial bins. Since a quasisteady-state configuration is achieved, the relative errors quoted above overestimate the actual error due small time-dependent fluctuations that are present at every given point when the simulation is stopped.

It is easy to see that small time-dependent fluctuations are the main source of the error by investigating the error without averaging over the angle. Figure 10 shows the
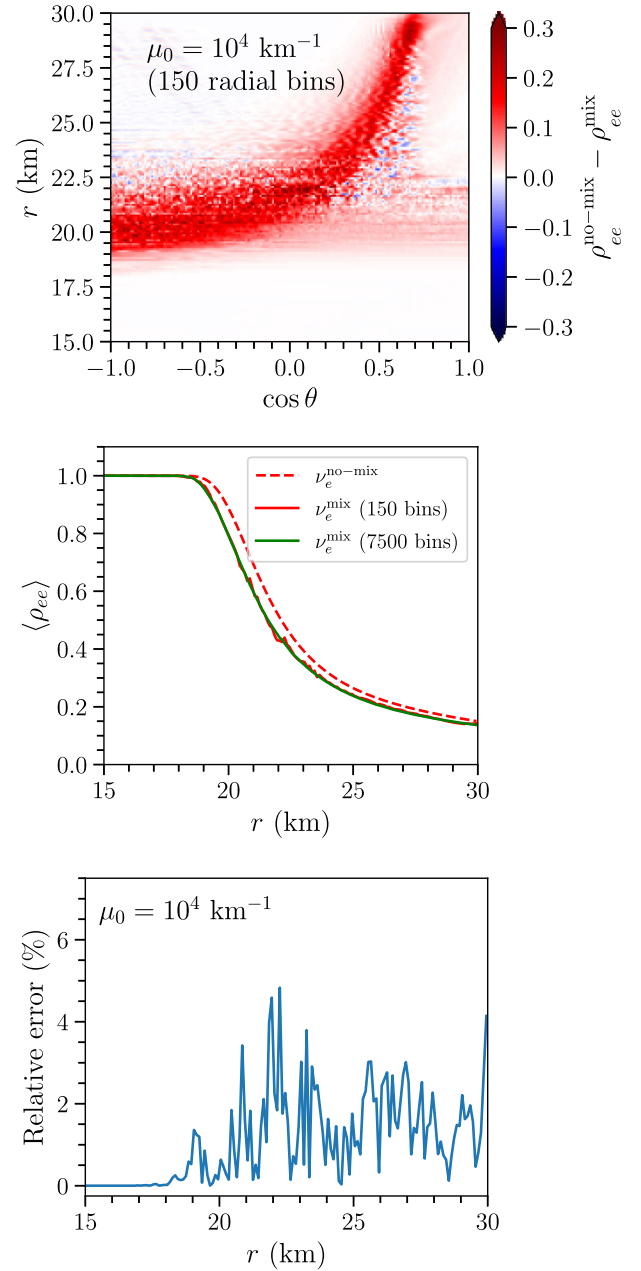

FIG. 8. Comparison between simulations with a different number of radial bins for $\mu_0 = 10^4$ km^{-1}. The top panel shows the difference between ρ_{ee} with and without mixing for $\mu_0 = 10^4$ km^{-1} computed using 150 spatial bins. The middle panel shows the initial angle averaged ρ_{ee} as red-dashed line. The red-solid line and green solid line shows are the angle averaged ρ_{ee} calculated using 150 and 7500 spatial bins. The red solid line is difficult to see due to the overlap with the green solid line. The bottom panel shows the relative error between the two simulations as a function of r. The overall error averaged over radius is 1.1%.

absolute error in $\rho_{ee}^{\mathrm{mix}} - \rho_{ee}^{\mathrm{no-mix}}$ in the left panel and the relative error in the right panel for the simulations with $\mu_0 = 10^4$ km^{-1} (see also Figs. 4 and 8).
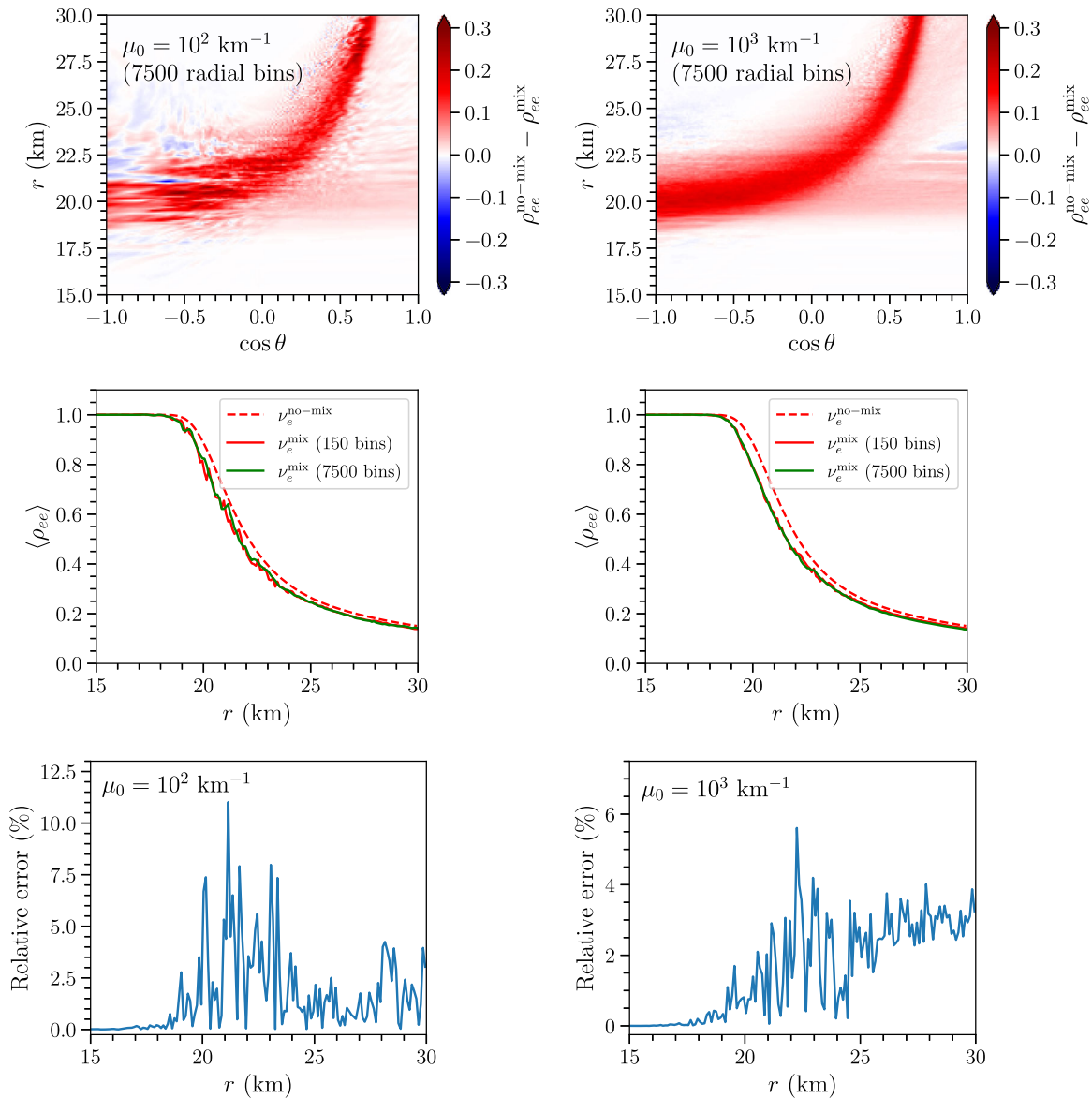
FIG. 9. Same as Fig. 8 but with $\mu_0 = 10^2$ km^{-1} (left) and $\mu_0 = 10^3$ km^{-1} (right).
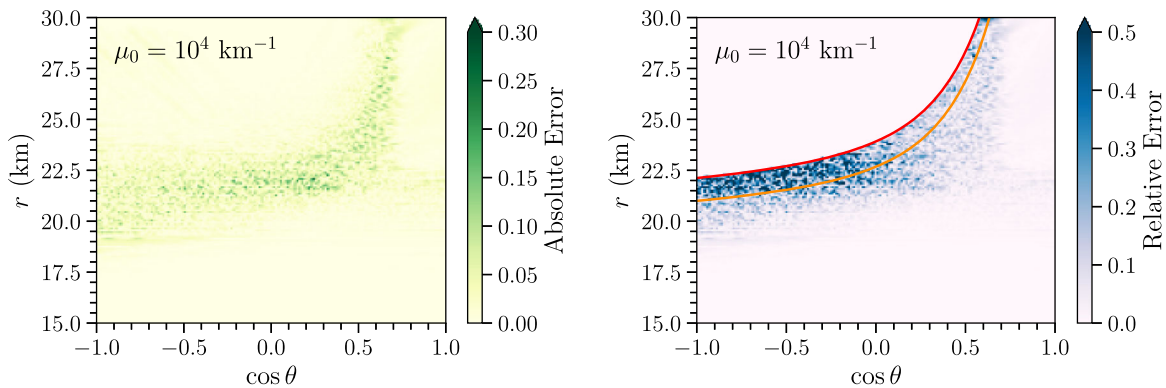

FIG. 10. Left: Absolute error in $\rho_{ee}^{\text{no-mix}} - \rho_{ee}^{\text{mix}}$ in the plane spanned by $\cos\theta$ and r, and for $\mu_0 = 10^4$ km^{-1}. The error has been obtained by comparing the coarse grained results of the simulation with 7500 spatial bins with the results of the simulation with 150 spatial bins. Right: Relative error in ρ_{ee}^{mix} for regions where $\rho_{ee}^{\text{no-mix}}$ is greater than 0.1. For reference, the loci of points where $\rho_{ee}^{\text{no-mix}}$ is equal to 0.1 and 0.5 are shown in red and orange, respectively.
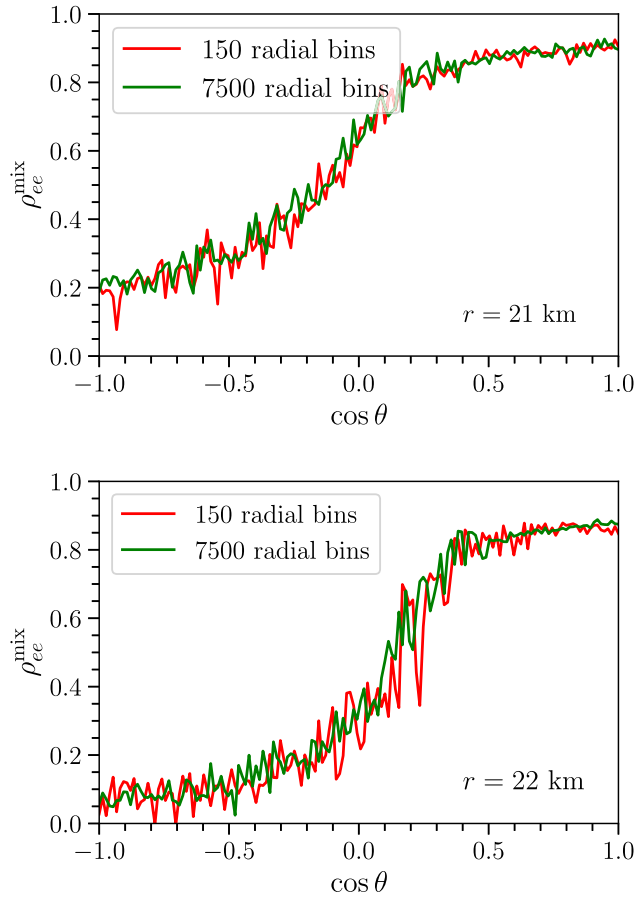
FIG. 11. Angular distributions of ν_e after flavor conversion, extracted at $r = 21$ and $r = 22$ km and for $\mu_0 = 10^4$ km^{-1} for the simulations with 150 (red) and 7500 (green) radial bins. The two curves are in very good agreement.

The absolute error in the left panel of Fig. 10 provides an accurate representation of the error in our simulation, which is about 0.1–0.15 throughout the simulation domain. The relative error is shown in the right panel of Fig. 10 for completeness. We plot the relative error only for the regions where $\rho_{ee}^{\text{no}-\text{mix}} \gtrsim 0.1$ (see red contour in the right panel of Fig. 10). To guide the eye, we also show an orange contour where $\rho_{ee}^{\text{no}-\text{mix}} \simeq 0.5$. The right panel shows that the relative error between the low- and high-resolution simulations is less than 5–10%. However, it can reach up to 40% for $\cos \theta < 0$ where the relative error is not an informative quantity since there are very few neutrinos in the tail of the angular distribution. We stress that the relative error is ill-defined in such regions and should be considered with extreme caution. This becomes clear by looking at Fig. 11 where we show the ν_e angular distribution when the quasisteady state is reached for $r = 21$ and $r = 22$ km with $\mu_0 = 10^4$ km^{-1}. We plot ρ_{ee}^{mix} obtained from the simulation with 150 spatial bins, alongside with the correspondent angular distributions obtained from the simulation with 7500 spatial bins. The angular distributions obtained for the
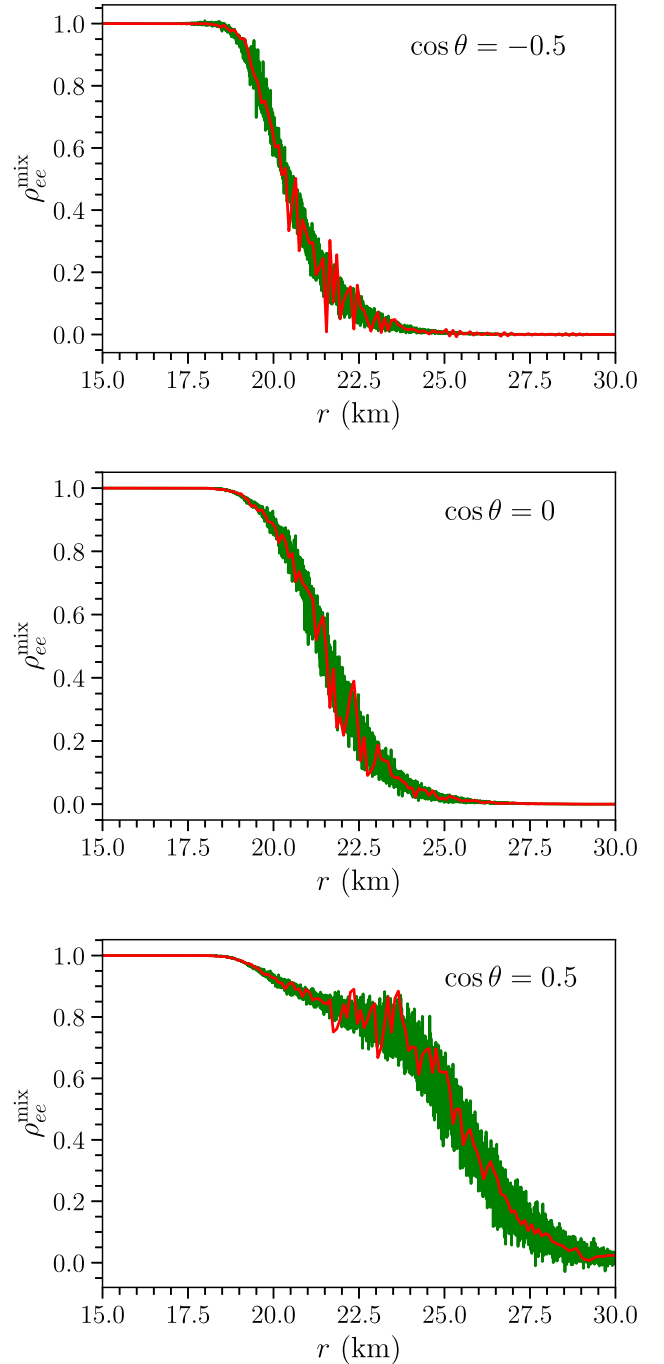

FIG. 12. Radial profile of ρ_{ee} after flavor conversion, extracted at $\cos \theta = -0.5$, 0, and 0.5 (from top to bottom, respectively) for $\mu_0 = 10^4$ km^{-1} for the simulations with 150 (red) and 7500 (green) spatial bins.

simulations with 150 bins and 7500 bins are in very good agreement, yet if one were to compute the relative error e.g., for $\cos \theta = -0.9$, one would obtain an error above 40%; this clearly shows the misleading information provided by the relative error in the right panel of Fig. 10 for some regions of the parameter space spanned by $\cos \theta$ and r.

Figure 12 shows the radial evolution of ρ_{ee}^{mix} obtained from the simulations with 150 and 7500 spatial bins for $\cos\theta = -0.5$, 0, and 0.5 (from top to bottom panels, respectively). One can clearly see that the low-resolution curve tracks the average behavior of the high-resolution one.

It is worth highlighting that the value of μ_0 reported above is the self-interaction strength at $r_{\min}$; as neutrinos start decoupling, the effective strength of self-interaction decreases as the fourth power of the radius, which is automatically taken into account in our simulations.

[1] Adam Burrows and David Vartanyan, Core-collapse supernova explosion theory, Nature (London) **589**, 29 (2021).

[2] Hans-Thomas Janka, Tobias Melson, and Alexander Summa, Physics of core-collapse supernovae in three dimensions: A sneak preview, Annu. Rev. Nucl. Part. Sci. **66**, 341 (2016).

[3] Stirling A. Colgate and Richard H. White, The hydrodynamic behavior of supernovae explosions, Astrophys. J. **143**, 626 (1966).

[4] James R. Wilson, Supernovae and post-collapse behavior, in *Numerical Astrophysics* (Jones and Bartlett Publications, Boston, 1985), p. 422, https://ui.adsabs.harvard.edu/abs/1985nuas.conf..422W/abstract.

[5] Hans A. Bethe and James R. Wilson, Revival of a stalled supernova shock by neutrino heating, Astrophys. J. **295**, 14 (1985).

[6] Maximilian Ruffert, Hans-Thomas Janka, Koh Takahashi, and Gerhard Schaefer, Coalescing neutron stars: A step towards physical models. 2. Neutrino emission, neutron tori, and gamma-ray bursts, Astron. Astrophys. **319**, 122 (1997), https://inspirehep.net/literature/420239.

[7] Robert Popham, Stan E. Woosley, and Christopher Fryer, Hyperaccreting black holes and gamma-ray bursts, Astrophys. J. **518**, 356 (1999).

[8] Andrei M. Beloborodov, Nuclear composition of gamma-ray burst fireballs, Astrophys. J. **588**, 931 (2003).

[9] Maximilian Ruffert and Hans-Thomas Janka, Gamma-ray bursts from accreting black holes in neutron star mergers, Astron. Astrophys. **344**, 573 (1999), https://inspirehep.net/literature/477427.

[10] Oliver Just, Martin Obergaulinger, H. Thomas Janka, Andreas Bauswein, and Nicole Schwarz, Neutron-star merger ejecta as obstacles to neutrino-powered jets of gamma-ray bursts, Astrophys. J. Lett. **816**, L30 (2016).

[11] John J. Cowan, Christopher Sneden, James E. Lawler, Ani Aprahamian, Michael Wiescher, Karlheinz Langanke, Gabriel Martínez-Pinedo, and Friedrich-Karl Thielemann, Origin of the heaviest elements: The rapid neutron-capture process, Rev. Mod. Phys. **93**, 015002 (2021).

[12] Dimitri Mihalas, Barbara Weibel Mihalas, Albert Fu, and W. David Arnett, *Foundations of Radiation Hydrodynamics* (Oxford University Press, New York, 1985).

[13] Anthony Mezzacappa, Eirik Endeve, O. E. Bronson Messer, and Stephen W. Bruenn, Physical, numerical, and computational challenges of modeling neutrino transport in core-collapse supernovae, Living Rev. Comput. Astrophys. **6**, 4 (2020).

[14] Masaru Shibata and Kenta Hotokezaka, Merger and mass ejection of neutron-star binaries, Annu. Rev. Nucl. Part. Sci. **69**, 41 (2019).

[15] Francois Foucart, Neutrino transport in general relativistic neutron star merger simulations, Living Rev. Comput. Astrophys. **9**, 1 (2023).

[16] Rodrigo Fernández, Sherwood Richers, Nicole Mulyk, and Steven Fahlman, Fast flavor instability in hypermassive neutron star disk outflows, Phys. Rev. D **106**, 103003 (2022).

[17] Günther Sigl and Georg G. Raffelt, General kinetic description of relativistic mixed neutrinos, Nucl. Phys. **B406**, 423 (1993).

[18] Alexey Vlasenko, George M. Fuller, and Vincenzo Cirigliano, Neutrino quantum kinetics, Phys. Rev. D **89**, 105004 (2014).

[19] Alexey Vlasenko, George M. Fuller, and Vincenzo Cirigliano, Prospects for neutrino-antineutrino transformation in astrophysical environments, arXiv:1406.6724.

[20] Julien Serreau and Cristina Volpe, Neutrino-antineutrino correlations in dense anisotropic media, Phys. Rev. D **90**, 125040 (2014).

[21] Daniel N. Blaschke and Vincenzo Cirigliano, Neutrino quantum kinetic equations: The collision term, Phys. Rev. D **94**, 033009 (2016).

[22] Huaiyu Duan, George M. Fuller, and Yong-Zhong Qian, Collective neutrino oscillations, Annu. Rev. Nucl. Part. Sci. **60**, 569 (2010).

[23] Alessandro Mirizzi, Irene Tamborra, Hans-Thomas Janka, Ninetta Saviano, Kate Scholberg, Robert Bollig, Lorenz Hüdepohl, and Sovan Chakraborty, Supernova neutrinos: Production, oscillations and detection, Riv. Nuovo Cimento **39**, 1 (2016).

[24] Irene Tamborra and Shashank Shalgar, New developments in flavor evolution of a dense neutrino gas, Annu. Rev. Nucl. Part. Sci. **71**, 165 (2021).

[25] James T. Pantaleone, Neutrino oscillations at high densities, Phys. Lett. B **287**, 128 (1992).

[26] Huaiyu Duan, George M. Fuller, and Yong-Zhong Qian, Collective neutrino flavor transformation in supernovae, Phys. Rev. D **74**, 123004 (2006).

[27] Huaiyu Duan, George M. Fuller, J. Carlson, and Yong-Zhong Qian, Simulation of coherent non-linear neutrino flavor transformation in the supernova environment. 1. Correlated neutrino trajectories, Phys. Rev. D **74**, 105014 (2006).

[28] Huaiyu Duan, George M. Fuller, J. Carlson, and Yong-Zhong Qian, Coherent Development of Neutrino Flavor in

the Supernova Environment, Phys. Rev. Lett. **97,** 241101 (2006).

[29] Gianluigi Fogli, Eligio Lisi, Antonio Marrone, and Alessandro Mirizzi, Collective neutrino flavor transitions in supernovae and the role of trajectory averaging, J. Cosmol. Astropart. Phys. 12 (2007) 010.

[30] Steen Hannestad, Georg G. Raffelt, Gunter Sigl, and Yvonne Y. Y. Wong, Self-induced conversion in dense neutrino gases: Pendulum in flavour space, Phys. Rev. D **74,** 105010 (2006); **76,** 029901(E) (2007).

[31] Basudeb Dasgupta, Evan P. O'Connor, and Christian D. Ott, The role of collective neutrino flavor oscillations in core-collapse supernova shock revival, Phys. Rev. D **85,** 065008 (2012).

[32] Raymond F. Sawyer, Speed-up of neutrino transformations in a supernova environment, Phys. Rev. D **72,** 045003 (2005).

[33] Raymond F. Sawyer, The multi-angle instability in dense neutrino systems, Phys. Rev. D **79,** 105003 (2009).

[34] Raymond F. Sawyer, Neutrino Cloud Instabilities Just Above the Neutrino Sphere of a Supernova, Phys. Rev. Lett. **116,** 081101 (2016).

[35] Sovan Chakraborty, Rasmus Sloth Hansen, Ignacio Izaguirre, and Georg G. Raffelt, Self-induced neutrino flavor conversion without flavor mixing, J. Cosmol. Astropart. Phys. 03 (2016) 042.

[36] Ignacio Izaguirre, Georg G. Raffelt, and Irene Tamborra, Fast Pairwise Conversion of Supernova Neutrinos: A Dispersion-Relation Approach, Phys. Rev. Lett. **118,** 021101 (2017).

[37] Irene Tamborra, Lorenz Hüdepohl, Georg G. Raffelt, and Hans-Thomas Janka, Flavor-dependent neutrino angular distribution in core-collapse supernovae, Astrophys. J. **839,** 132 (2017).

[38] Sajad Abbar, Huaiyu Duan, Kohsuke Sumiyoshi, Tomoya Takiwaki, and Maria Cristina Volpe, On the occurrence of fast neutrino flavor conversions in multidimensional supernova models, Phys. Rev. D **100,** 043004 (2019).

[39] Milad Delfan Azari, Shoichi Yamada, Taiki Morinaga, Wakana Iwakami, Hirotada Okawa, Hiroki Nagakura, and Kohsuke Sumiyoshi, Linear analysis of fast-pairwise collective neutrino oscillations in core-collapse supernovae based on the results of Boltzmann simulations, Phys. Rev. D **99,** 103011 (2019).

[40] Taiki Morinaga, Hiroki Nagakura, Chinami Kato, and Shoichi Yamada, Fast neutrino-flavor conversion in the preshock region of core-collapse supernovae, Phys. Rev. Res. **2,** 012046 (2020).

[41] Milad Delfan Azari, Shoichi Yamada, Taiki Morinaga, Hiroki Nagakura, Shun Furusawa, Akira Harada, Hirotada Okawa, Wakana Iwakami, and Kohsuke Sumiyoshi, Fast collective neutrino oscillations inside the neutrino sphere in core-collapse supernovae, Phys. Rev. D **101,** 023018 (2020).

[42] Hiroki Nagakura, Taiki Morinaga, Chinami Kato, and Shoichi Yamada, Fast-pairwise collective neutrino oscillations associated with asymmetric neutrino emissions in core-collapse supernovae, Astrophys. J. **886,** 139 (2019).

[43] Sajad Abbar, Huaiyu Duan, Kohsuke Sumiyoshi, Tomoya Takiwaki, and Maria Cristina Volpe, Fast neutrino flavor conversion modes in multidimensional core-collapse supernova models: The role of the asymmetric neutrino distributions, Phys. Rev. D **101,** 043016 (2020).

[44] Robert Glas, Hans-Thomas Janka, Francesco Capozzi, Manibrata Sen, Basudeb Dasgupta, Alessandro Mirizzi, and Guenter Sigl, Fast neutrino flavor instability in the neutron-star convection layer of three-dimensional supernova models, Phys. Rev. D **101,** 063001 (2020).

[45] Francesco Capozzi, Sajad Abbar, Robert Bollig, and Hans-Thomas Janka, Fast neutrino flavor conversions in one-dimensional core-collapse supernova models with and without muon creation, Phys. Rev. D **103,** 063013 (2021).

[46] Hiroki Nagakura, Lucas Johns, Adam Burrows, and George M. Fuller, Where, when, and why: Occurrence of fast-pairwise collective neutrino oscillation in three-dimensional core-collapse supernova models, Phys. Rev. D **104,** 083025 (2021).

[47] Akira Harada and Hiroki Nagakura, Prospects of fast flavor neutrino conversion in rotating core-collapse supernovae, Astrophys. J. **924,** 109 (2022).

[48] Meng-Ru Wu and Irene Tamborra, Fast neutrino conversions: Ubiquitous in compact binary merger remnants, Phys. Rev. D **95,** 103007 (2017).

[49] Meng-Ru Wu, Irene Tamborra, Oliver Just, and Hans-Thomas Janka, Imprints of neutrino-pair flavor conversions on nucleosynthesis in ejecta from neutron-star merger remnants, Phys. Rev. D **96,** 123015 (2017).

[50] Manu George, Meng-Ru Wu, Irene Tamborra, Ricard Ardevol-Pulpillo, and Hans-Thomas Janka, Fast neutrino flavor conversion, ejecta properties, and nucleosynthesis in newly-formed hypermassive remnants of neutron-star mergers, Phys. Rev. D **102,** 103015 (2020).

[51] Oliver Just, Sajad Abbar, Meng-Ru Wu, Irene Tamborra, Hans-Thomas Janka, and Francesco Capozzi, Fast neutrino conversion in hydrodynamic simulations of neutrino-cooled accretion disks, Phys. Rev. D **105,** 083024 (2022).

[52] Xinyu Li and Daniel M. Siegel, Neutrino Fast Flavor Conversions in Neutron-Star Postmerger Accretion Disks, Phys. Rev. Lett. **126,** 251101 (2021).

[53] Taiki Morinaga, Fast neutrino flavor instability and neutrino flavor lepton number crossings, Phys. Rev. D **105,** L101301 (2022).

[54] Basudeb Dasgupta, Collective Neutrino Flavor Instability Requires a Crossing, Phys. Rev. Lett. **128,** 081102 (2022).

[55] Shashank Shalgar and Irene Tamborra, Dispelling a myth on dense neutrino media: Fast pairwise conversions depend on energy, J. Cosmol. Astropart. Phys. 01 (2021) 014.

[56] Shashank Shalgar, Ian Padilla-Gay, and Irene Tamborra, Neutrino propagation hinders fast pairwise flavor conversions, J. Cosmol. Astropart. Phys. 06 (2020) 048.

[57] Shashank Shalgar and Irene Tamborra, Three flavor revolution in fast pairwise neutrino conversion, Phys. Rev. D **104,** 023011 (2021).

[58] Lucas Johns, Hiroki Nagakura, George M. Fuller, and Adam Burrows, Neutrino oscillations in supernovae: Angular moments and fast instabilities, Phys. Rev. D **101,** 043009 (2020).

[59] Madhurima Chakraborty and Sovan Chakraborty, Three flavor neutrino conversions in supernovae: Slow & fast instabilities, J. Cosmol. Astropart. Phys. 01 (2020) 005.

[60] Basudeb Dasgupta, Alessandro Mirizzi, and Manibrata Sen, Fast neutrino flavor conversions near the supernova core with realistic flavor-dependent angular distributions, J. Cosmol. Astropart. Phys. 02 (2017) 019.

[61] Ian Padilla-Gay, Irene Tamborra, and Georg G. Raffelt, Neutrino Flavor Pendulum Reloaded: The Case of Fast Pairwise Conversion, Phys. Rev. Lett. **128,** 121102 (2022).

[62] Gordon E. Brown, Hans A. Bethe, and Gordon Baym, Supernova theory, Nucl. Phys. **A375,** 481 (1982).

[63] Shashank Shalgar and Irene Tamborra, On the occurrence of crossings between the angular distributions of electron neutrinos and antineutrinos in the supernova core, Astrophys. J. **883,** 80 (2019).

[64] Shashank Shalgar and Irene Tamborra, A change of direction in pairwise neutrino conversion physics: The effect of collisions, Phys. Rev. D **103,** 063002 (2021).

[65] Rasmus S. L. Hansen, Shashank Shalgar, and Irene Tamborra, Enhancement or damping of fast neutrino flavor conversions due to collisions, Phys. Rev. D **105,** 123003 (2022).

[66] Hirokazu Sasaki and Tomoya Takiwaki, A detailed analysis of the dynamics of fast neutrino flavor conversions with scattering effects, Prog. Theor. Exp. Phys. **2022,** 073E01 (2022).

[67] Joshua D. Martin, Joseph Carlson, Vincenzo Cirigliano, and Huaiyu Duan, Fast flavor oscillations in dense neutrino media with collisions, Phys. Rev. D **103,** 063001 (2021).

[68] Francesco Capozzi, Basudeb Dasgupta, Alessandro Mirizzi, Manibrata Sen, and Günter Sigl, Collisional Triggering of Fast Flavor Conversions of Supernova Neutrinos, Phys. Rev. Lett. **122,** 091101 (2019).

[69] Lucas Johns, Collisional Flavor Instabilities of Supernova Neutrinos, Phys. Rev. Lett. **130,** 191001 (2023).

[70] Sherwood A. Richers, Gail C. McLaughlin, James P. Kneller, and Alexey Vlasenko, Neutrino quantum kinetics in compact objects, Phys. Rev. D **99,** 123014 (2019).

[71] Sherwood Richers, Donald Willcox, and Nicole Ford, Neutrino fast flavor instability in three dimensions, Phys. Rev. D **104,** 103023 (2021).

[72] Francesco Capozzi, Madhurima Chakraborty, Sovan Chakraborty, and Manibrata Sen, Fast Flavor Conversions in Supernovae: The Rise of mu-tau Neutrinos, Phys. Rev. Lett. **125,** 251801 (2020).

[73] Francesco Capozzi, Madhurima Chakraborty, Sovan Chakraborty, and Manibrata Sen, Supernova fast flavor conversions in 1 + 1D: Influence of mu-tau neutrinos, Phys. Rev. D **106,** 083011 (2022).

[74] Guenther Sigl and Georg G. Raffelt, General kinetic description of relativistic mixed neutrinos, Nucl. Phys. **B406,** 423 (1993).

[75] Markus Rampp and Hans-Thomas Janka, Radiation hydrodynamics with neutrinos: Variable Eddington factor method for core collapse supernova simulations, Astron. Astrophys. **396,** 361 (2002).

[76] Hiroki Nagakura, General-relativistic quantum-kinetics neutrino transport, Phys. Rev. D **106,** 063011 (2022).

[77] Andreu Esteban-Pretel, Alessandro Mirizzi, Sergio Pastor, Ricard Tomàs, Georg G. Raffelt, Pasquale D. Serpico, and Guenther Sigl, Role of dense matter in collective supernova neutrino transformations, Phys. Rev. D **78,** 085012 (2008).

[78] Steven Weinberg, *Lectures on Astrophysics* (Cambridge University Press, Cambridge, England, 2019), 10.1017/9781108227445.

[79] Robert L. Bowers and James R. Wilson, A numerical model for stellar core collapse calculations, Astrophys. J. Suppl. Ser. **50,** 115 (1982).

[80] Evan O'Connor, An open-source neutrino radiation hydrodynamics code for core-collapse supernovae, Astrophys. J. Suppl. Ser. **219,** 24 (2015).

[81] Stephen W. Bruenn, Stellar core collapse—numerical model and infall epoch, Astrophys. J. Suppl. Ser. **58,** 771 (1985).

[82] Georg G. Raffelt, *Stars as Laboratories for Fundamental Physics* (The University of Chicago Press, Chicago, 1996).

[83] Shashank Shalgar and Irene Tamborra, Neutrino flavor conversion, advection, and collisions: Toward the full solution, Phys. Rev. D **107,** 063025 (2023).

[84] Mathias Th. Keil, Georg G. Raffelt, and Hans-Thomas Janka, Monte Carlo study of supernova neutrino spectra formation, Astrophys. J. **590,** 971 (2003).

[85] Georg G. Raffelt, Mathias Th. Keil, Robert Buras, Hans-Thomas Janka, and Markus Rampp, Supernova neutrinos: Flavor-dependent fluxes and spectra, in *Proceedings of the 4th Workshop on Neutrino Oscillations and their Origin (NOON2003)* (2003), pp. 380–387, arXiv:astro-ph/0303226.

[86] Christian D. Ott, Adam Burrows, Luc Dessart, and Eli Livne, 2D multi-angle, multi-group neutrino radiation-hydrodynamic simulations of postbounce supernova cores, Astrophys. J. **685,** 1069 (2008).

[87] Meng-Ru Wu, Manu George, Chun-Yu Lin, and Zewei Xiong, Collective fast neutrino flavor conversions in a 1D box: Initial conditions and long-term evolution, Phys. Rev. D **104,** 103003 (2021).

[88] Leo Stodolsky, Neutron optics and weak currents, Phys. Lett. **50B,** 352 (1974).

[89] Robert A. Harris and Leo Stodolsky, Two state systems in media and 'Turing's Paradox', Phys. Lett. **116B,** 464 (1982).

[90] Leo Stodolsky, On the treatment of neutrino oscillations in a thermal environment, Phys. Rev. D **36,** 2273 (1987).

[91] Arka Banerjee, Amol Dighe, and Georg G. Raffelt, Linearized flavor-stability analysis of dense neutrino streams, Phys. Rev. D **84,** 053013 (2011).

[92] Vincenzo Cirigliano, Mark W. Paris, and Shashank Shalgar, Effect of collisions on neutrino flavor inhomogeneity in a dense neutrino gas, Phys. Lett. B **774,** 258 (2017).

[93] Ian Padilla-Gay, Shashank Shalgar, and Irene Tamborra, Multi-dimensional solution of fast neutrino conversions in binary neutron star merger remnants, J. Cosmol. Astropart. Phys. 01 (2021) 017.

[94] Sherwood Richers, Don E. Willcox, Nicole M. Ford, and Andrew Myers, Particle-in-cell simulation of the neutrino fast flavor instability, Phys. Rev. D **103,** 083013 (2021).

[95] Sherwood Richers, Huaiyu Duan, Meng-Ru Wu, Soumya Bhattacharyya, Masamichi Zaizen, Manu George, Chun-Yu Lin, and Zewei Xiong, Code comparison for fast flavor instability simulations, Phys. Rev. D **106,** 043011 (2022).

[96] Soumya Bhattacharyya and Basudeb Dasgupta, Fast Flavor Depolarization of Supernova Neutrinos, Phys. Rev. Lett. **126**, 061302 (2021).

[97] Lucas Johns, Hiroki Nagakura, George M. Fuller, and Adam Burrows, Fast oscillations, collisionless relaxation, and spurious evolution of supernova neutrino flavor, Phys. Rev. D **102**, 103017 (2020).

[98] Shashank Shalgar and Irene Tamborra, Symmetry breaking induced by pairwise conversion of neutrinos in compact sources, Phys. Rev. D **105**, 043018 (2022).

[99] Huaiyu Duan and Shashank Shalgar, Flavor instabilities in the neutrino line model, Phys. Lett. B **747**, 139 (2015).